J. Fluid Mech. (2008), *vol.* 599, *pp.* 81–110.
doi:10.1017/S0022112007009986 Printed in the United Kingdom

Gaseous detonation propagation in a bifurcated tube

C. J. WANG, S. L. XU AND C. M. GUO

Department of Mechanics and Mechanical Engineering, University of Science and Technology of China, Hefei 230026, Anhui, China *and* State Key laboratory of Explosion Science and Technology, Beijing Institute of Technology, Beijing 100081, China

(Received 14 July 2005 and in revised form 14 November 2007)

Gaseous detonation propagation in a bifurcated tube was experimentally and numerically studied for stoichiometric hydrogen and oxygen mixtures diluted with argon. Pressure detection, smoked foil recording and schlieren visualization were used in the experiments. Numerical simulation was carried out at low initial pressure (8.00 kPa), based on the reactive Navier–Stokes equations in conjunction with a detailed chemical reaction model. The results show that the detonation wave is strongly disturbed by the wall geometry of the bifurcated tube and undergoes a successive process of attenuation, failure, re-initiation and the transition from regular reflection to Mach reflection. Detonation failure is attributed to the rarefaction waves from the left-hand corner by decoupling leading shock and reaction zones. Re-initiation is induced by the inert leading shock reflection on the right-hand wall in the vertical branch. The branched wall geometry has only a local effect on the detonation propagation. In the horizontal branch, the disturbed detonation wave recovers to a self-sustaining one earlier than that in the vertical branch. A critical case was found in the experiments where the disturbed detonation wave can be recovered to be self-sustaining downstream of the horizontal branch, but fails in the vertical branch, as the initial pressure drops to 2.00 kPa. Numerical simulation also shows that complex vortex structures can be observed during detonation diffraction. The reflected shock breaks the vortices into pieces and its interaction with the unreacted recirculation region induces an embedded jet. In the vertical branch, owing to the strength difference at any point and the effect of chemical reactions, the Mach stem cannot be approximated as an arc. This is different from the case in non-reactive steady flow. Generally, numerical simulation qualitatively reproduces detonation attenuation, failure, re-initiation and the transition from regular reflection to Mach reflection observed in experiments.

1. Introduction

It is well known that gaseous hydrocarbon fuels are transported by pipelines in the energy and chemical engineering industries. Usually there exists a great variety of bends, bifurcated and circular tubes, valves, joints, etc. Upon accidental ignition, gaseous deflagration or even detonation may occur and result in serious economic losses and casualties. Additionally, methane or methane-dust explosions often happen in coal mining industries. Thus, since the bifurcated tube is relatively common, study of gaseous detonation propagation through it is important and the challenge is to suppress or prevent explosion hazards. In the academic sense, much work has already been performed on gaseous detonation propagation in a straight tube. The essential

interest focuses on the coupling between the reaction zone and the leading shock wave. The phenomenon of gaseous detonation propagation in a non-straight tube such as a bifurcated one is much more complicated and challenging because of the effect of the wall geometry. The wall geometry affects the leading shock strength as well as the temperature behind the shock wave and further determines the chemical reaction rate. This leads to some complicated physical phenomena such as detonation diffraction, reflection, failure and re-initiation.

Most previous studies focus on the multi-dimensional structure and cellular dynamics of detonation waves (White 1961; Bourlioux, Majda & Roytburd 1991; Oran *et al.* 1998) and the interaction between detonation and obstacles in a straight tube (Zhou, Li & Chen 1990; Zhou & Li 1997; Guo, Thomas & Zhang 2002; Radulescu & Lee 2002). There are some investigations on Mach reflection of detonation on a wedge (Akbar 1997; Ohyagi *et al.* 2000; Guo, Zhang & Xie 2001) and diffraction around an abrupt area change (Edwards & Thomas 1979; Bartlmä & Schröder 1986; Jones *et al.* 2000; Schultz 2000; Arienti & Shepherd 2005). Until now, only a relatively small amount of work has been conducted on gaseous detonation propagation through tubes with complex geometry. Thomas & Williams (2002) presented gaseous detonation interaction with bends. In a sharp bend, the detonation wave locally fails for a lower initial pressure, whereas the detonation wave continually propagates at a higher initial pressure. As the wall radius is increased, it becomes increasingly easier to maintain the cellular structure. Ohyagi *et al.* (2002) experimentally studied diffraction and re-initiation of detonations behind a backward-facing step. The re-initiation occurs at the bottom wall where the decoupled shock reflects. The re-initiated wave is an exploding detonation with a very small cell size. Li & Kailasanath (2000) numerically investigate detonation transmission from a small channel to a large one. The expansion waves weaken the detonation wave at the exit of the small channel. The reflected shocks from the walls in a large channel can create local regions of high pressure and temperature and therefore reignite the mixture near the walls.

Planar non-reactive shock propagation through a bifurcated tube was studied by Igra *et al.* (1998). They found that the interaction of the shock with the bifurcated segment results in a complex two-dimensional unsteady flow. Just after passing through the right-hand corner of the branched segment, the shock exhibits a Mach reflection mode in the horizontal branch and experiences the transition from the regular reflection to Mach reflection in the vertical branch. Finally, a weakened planar shock is generated. A gaseous detonation wave is not inherently planar, consisting of a leading shock and a reaction zone. The leading shock is made up of alternate weaker incident shocks and stronger Mach stems, joined at the triple points by transverse waves which sweep back and forth along the front and extend back into the reaction zone. Because of the effect of rarefaction waves from the sharp corner, detonation failure and re-initiation possibly occur during detonation propagation in a bifurcated tube. So, there are evident differences between a detonation wave and a non-reactive shock wave. This stimulates us to investigate detonation propagation in a bifurcated tube. In this paper, our experimental and numerical results address this phenomenon in detail and provide insight into the detonation dynamics involved in the interactions among the leading shock, reaction zone and wall geometry in a bifurcated tube.

2. Experimental methods

Experiments were performed in a detonation tube with $40\,\text{mm} \times 40\,\text{mm}$ square cross-section and wall thickness of 5 mm. This tube consists of five sections: a 0.5 m driver section I, two driven sections II and III with length of 2.5 m and 2.0 m,

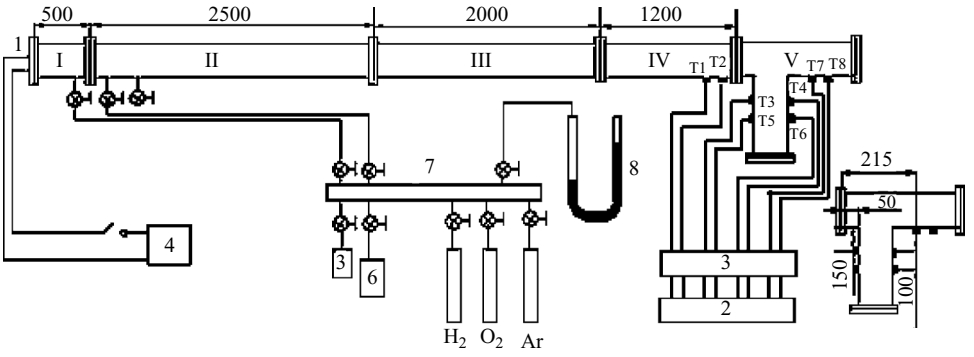

FIGURE 1. Schematic of experimental facilities. 1. Spark plug. 2. Digital oscilloscope. 3. Charge amplifier. 4. AC power. 5. Premixed gas tank. 6. Vacuum pump. 7. Gas distributor. 8. Vacuum gauge. T1–T8 piezo-electric transducers; I, driver section; II, III, driven sections; IV, V, test sections.

respectively, and test sections IV and V (figure 1). A thin diaphragm separates sections I and II, when a detonation wave generated at high initial pressure in the driver section is employed to ignite the gas mixture at low initial pressure in the driven section. Transducers T1 to T8 are mounted on test sections IV and V to record pressure history and then obtain the average speed of detonation propagation. Simultaneously, T2 is employed to trigger the ruby laser for flow visualization. The distance between T1 and the spark plug on the initiation end is 6.0 mm. A well-designed AC power source is used in the present study for spark ignition. High-voltage capacities of AC power with a total capacity of 200 μF are charged to a certain voltage ranging from 0 V to 30 kV, and a spark plug set at the left-hand end of the tube is triggered by a high-voltage pulse. In our experiments, the spark with an energy release of at least 20 J is required to ensure successful detonation initiation.

In order to avoid the disturbance of gaseous detonation self-luminescence, the laser-based schlieren system and a bandpass filter are used for flow visualization (figure 2). The light source is a Q-switched flash-lamp pumped ruby laser which creates a light pulse with approximately a 40 ns pulse width at a wavelength of 694.3 nm. The filter has a centreline of 694.3 nm and 15 nm FWHM (full wave at half maximum). The signal from the pressure transducer T2 is amplified to trigger the ruby laser source after a pre-determined time delay. The optical window has an available length of 170 mm and width of 110 mm for viewing. The distance from its left-hand edge to the corner L is 12 mm. Schlieren images with different time delays were taken from different experiments under the same initial conditions. The delay time possibly had a deficit within ± 2 μs. Because of the interest in the detonation front, a vertical knife edge was used so that the transverse waves propagating along the wavefront were not identified very clearly.

In addition, the smoked foils were also mounted on the sidewalls of test sections to obtain cellular patterns.

3. Physical and numerical models

3.1. *Governing equations and numerical methods*

Even though the detonation tube has a 40 mm × 40 mm square cross-section and is three-dimensional, the bifurcated segment has the same width as the upstream and

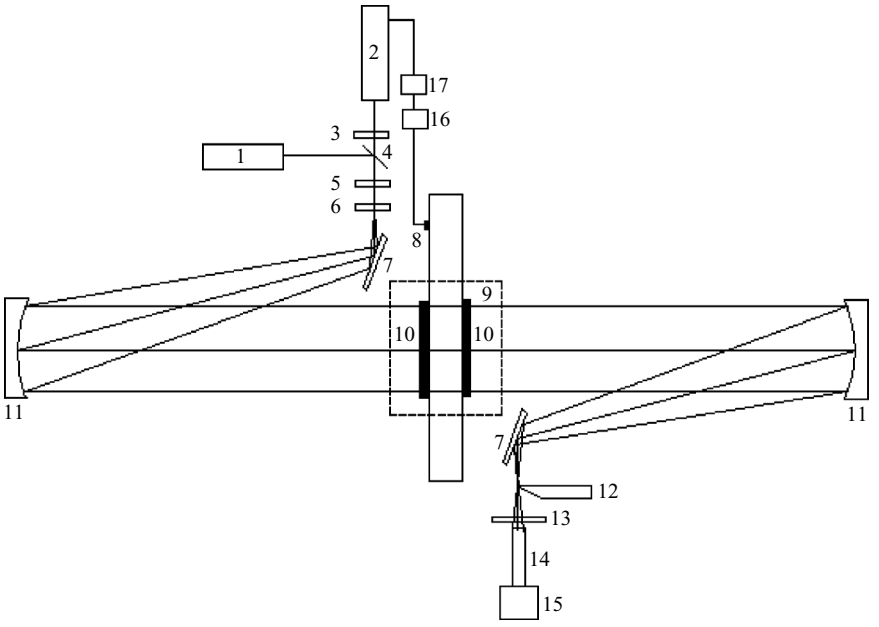

FIGURE 2. Schematic of the schlieren system. 1. He–Ne laser. 2. Ruby laser. 3. Light intensity adjustor. 4. Pellicle mirror. 5. Beam adjustor. 6. Beam expander. 7. Turning mirror. 8. Transducer. 9. Test section. 10. Windows. 11. Concave mirrors. 12. Knife edge. 13. Filter. 14. Object lens. 15. Camera. 16. Charge amplifier. 17. Delay generator.

downstream tubes. Furthermore, for a current with such high-speed reactive flow, the viscosity effects are relatively small. So the flow structure in the bifurcated tube is essentially two-dimensional. Two-dimensional multi-species (ns) reactive Navier–Stokes equations for such detonation problem can be employed and described as:

$$\frac{\partial Q}{\partial t}+\frac{\partial F}{\partial x}+\frac{\partial G}{\partial y}=\frac{1}{Re}\left(\frac{\partial F_v}{\partial x}+\frac{\partial G_v}{\partial y}\right)+S, \tag{3.1}$$

where

$$Q=\{\rho_1,\rho_2,\ldots,\rho_{NS},\rho u,\rho v,\rho E\}^T,$$
$$F=\{\rho_1 u,\rho_2 u,\ldots,\rho_{NS}u,\rho u^2+p,\rho uv,(\rho E+p)u\}^T,$$
$$G=\{\rho_1 v,\rho_2 v,\ldots,\rho_{NS}v,\rho uv,\rho v^2+p,(\rho E+p)v\}^T,$$
$$F_v=\left\{\rho D\frac{\partial Y_1}{\partial x},\rho D\frac{\partial Y_2}{\partial x},\ldots,\rho D\frac{\partial Y_{NS}}{\partial x},\tau_{xx},\tau_{yx},u\tau_{xx}+v\tau_{yx}+q_x\right\}^T,$$
$$G_v=\left\{\rho D\frac{\partial Y_1}{\partial y},\rho D\frac{\partial Y_2}{\partial y},\ldots,\rho D\frac{\partial Y_{NS}}{\partial y},\tau_{xy},\tau_{yy},u\tau_{xy}+v\tau_{yy}+q_y\right\}^T,$$
$$S=\{S_1,S_2,\ldots,S_{NS},0,0,0\}^T,$$
$$\tau_{xx}=\frac{2}{3}\mu\left(2\frac{\partial u}{\partial x}-\frac{\partial v}{\partial y}\right),\quad \tau_{yy}=\frac{2}{3}\mu\left(2\frac{\partial v}{\partial y}-\frac{\partial u}{\partial x}\right),$$
$$\tau_{xy}=\tau_{yx}=\mu\left(\frac{\partial u}{\partial y}+\frac{\partial v}{\partial x}\right),$$
$$q_x=\kappa\frac{\partial T}{\partial x}+\sum_{i=1}^{NS}\rho D_i h_i\frac{\partial Y_i}{\partial x},\quad q_y=\kappa\frac{\partial T}{\partial y}+\sum_{i=1}^{NS}\rho D_i h_i\frac{\partial Y_i}{\partial y},$$

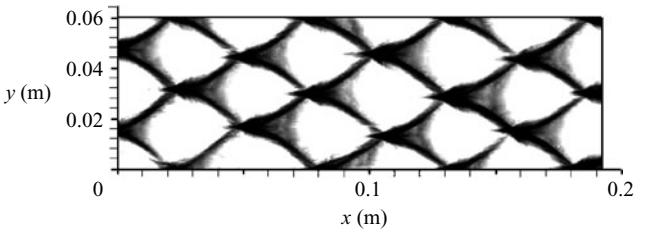

FIGURE 3. Time history of the local specific energy release.

where $\rho = \sum_{i=1}^{NS} \rho_i$, ρ_i is the ith species density. The ratio $Y_i = \rho_i/\rho$ denotes the ith species mass fraction. u and v are the velocity components in the x and y directions. p, T and E are pressure, temperature and the total energy per unit mass, respectively. S_i is the production rate of the ith species. h_i is the ith species enthalpy per unit mass. μ is viscosity coefficient, and κ is thermal conduction coefficient.

In the current study, an eight-species, forty-eight-reaction mechanism (Oran, Young & Boris 1982) is employed to describe the detonation chemical reaction for a stoichiometric hydrogen–oxygen–argon mixture. The reacting species are H_2, O_2, H, O, OH, HO_2, H_2O_2 and H_2O. The thermodynamic data come from the JANAF table (Gordon & McBride 1971).

The second-order additive semi-implicit Runge–Kutta Method (Zhong 1996) is employed to discretize the time term and treat the stiffness of the chemical source terms. Since the fine structures such as transverse waves, incident shocks, Mach stems, vortices and slip lines in the detonation flow field are highly and accurately resolved to avoid physical oscillations and excessive numerical dissipations, the convective terms of the governing equations are integrated by the fifth-order weighted essentially non-oscillatory (WENO) scheme (Shu & Osher 1988, 1989; Shu 1997). The viscosity, thermal conduction and molecular diffusion terms are evaluated using second-order central finite difference.

3.2. *Code validation*

The computational code involving the algorithm described above is numerically and experimentally validated in this paper. Section 4.3 provides numerical validation against our experimental results in the bifurcated tube. Here, the numerical validation is first performed by comparing our computational results in a straight channel with those obtained by Oran *et al.* (1998). Then a simple comparison to the experiment is also carried out.

A self-sustaining cellular detonation is simulated in the stoichiometric H_2–O_2 mixture diluted by 70% argon with an initial pressure of 6.67 kPa and an initial temperature of 298 K. All computational conditions such as channel width, grid size and initial values are completely consistent with those given by Oran *et al.* (1998), so our results can be compared directly with theirs (figure 3 and table 1). The final configuration is a mode four detonation. The cell size is approximately 54 mm × 30 mm, whereas Oran *et al.* predicted a somewhat larger cell size of 54 mm × 31 mm. The average speed of the self-sustaining detonation wave is 1595 m s^{-1}, slightly smaller than their value of 1625 m s^{-1}.

The current cell aspect ratio (the ratio of the width to the length in a detonation cell) is 0.54, which is in remarkable agreement with the experimental value of 0.53 or 0.54 (Eckett 2001). Compared to the Chapman–Jouguet (CJ) detonation speed of 1617.4 m s^{-1} predicted by the Gordon–McBride code (Gordon & McBride 1971), the

Study	Grid size	Δx (mm)	Δy (mm)	Average speed ($m\,s^{-1}$)	Equilibrium mode number	Cell size W (mm) × L (mm)
Current study	2048×256	0.15	0.235	1595	4	30×54
Oran *et al.*	2048×256	0.15	0.235	1625	4	31×54

TABLE 1. Comparison between the current and Oran *et al.*'s results for self-sustaining detonation waves ($2H_2 + O_2 + 7Ar$, $p_0 = 6.67$ kPa, $T_0 = 298$ K).

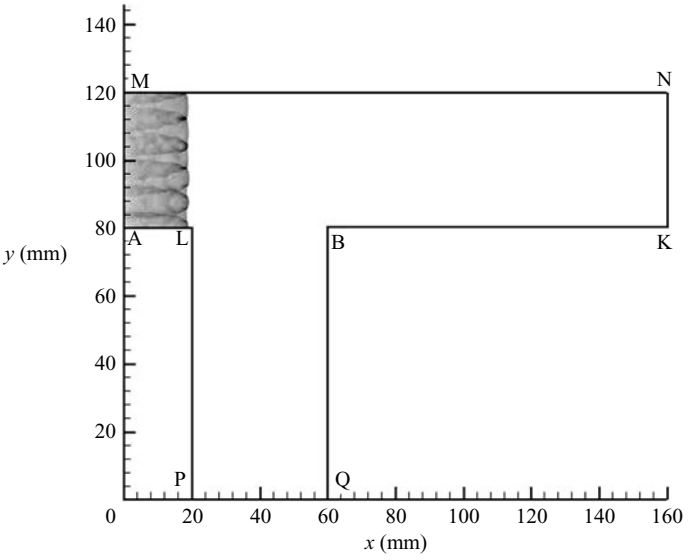

FIGURE 4. Schematic of computed domain.

current detonation speed is only 1.4% different. Furthermore, it is also consistent with the experimental value of $1550\,m\,s^{-1}$ (Eckett 2001).

In general, the current simulation duplicates Oran *et al.*'s perfectly, and it agrees well with the experiments.

3.3. *Computational set-up and initiation*

The computed domain (figure 4) was the same as that studied in experiments. This domain extended 160 mm in the x-direction and 120 mm in the y-direction. A two-dimensional rectangular Cartesian grid was imposed on our calculation. The grid spacing was uniform with $\Delta x = \Delta y = 0.1$ mm. The computations simulated a detonation wave propagating in the stoichiometric mixture of hydrogen and oxygen diluted by 25% argon at an initial pressure of 8.00 kPa and temperature of 300 K. Experience has shown that a more realistic way of initiating the computation was to use a detonation wave with a well-developed cellular structure upstream of the bifurcation segment. This cellular detonation wave was developed by perturbing a steady Zel'dovich–von Neumann–Doering (ZND) wave and letting it propagate until the average velocity reached a steady value that was essentially close to the CJ value.

4. Results and discussion

4.1. *Experimental results*

Figure 5 sequentially presents schlieren images, highlighting the phenomena of gaseous detonation propagation in a bifurcated tube. The tested gas mixture is $2H_2 + O_2$ with 25% argon dilution at an initial pressure of 16.00 kPa. The detonation wave travels from left to right. The cellular pattern at the same condition is shown in figure 6(*b*). It consists of three parts: the self-sustaining cellular patterns in the upstream region of the bifurcated segment and in the downstream region far away from the bifurcated segment, and the disturbed patterns in the horizontal and vertical branches. Figure 6(*a*) shows an enlarged image of the cellular pattern of the vertical branch in the vicinity of the bifurcated segment. Figure 6(*c*) shows related regions corresponding to the cellular pattern presented by figure 6(*b*). Seven different regions are demonstrated.

In figure 5(*a*), the detonation wave propagates in a self-sustaining state upstream of the bifurcated segment, where the cells which are closer to uniform than elsewhere in the system are observed in region 1 in figure 6. Because of low initial pressure and the integration effect of the schlieren technique, the wavefront and reaction zone seem a little thick. In figures 5(*b*) to 5(*d*), as soon as detonation diffracts around a 90° sharp corner (point L), owing to the effects of centred rarefaction waves emitted from point L, the pressure behind the leading shock drops and the wavefront is curved. Simultaneously, owing to the sudden area expansion, the transverse waves in this region miss the collision with their partners or the wall. As a result, they decay and then disappear. The reaction zone is gradually detached from the leading shock. Consequently, the latter has a fairly smooth appearance. The lower pressure behind the leading shock results in the larger cells in region 2 because of the lower reaction rates. Line NC marks the boundary between the regions with equilibrium and larger cells, as shown in figure 6. However, NC is not representative of the first characteristic line of the rarefaction waves because the leading shock of cellular detonation is not a completely planar shock. Point N may be upstream of, or just at, the left-hand corner, owing to the randomness of cell formation or DDT (deflagration-to-detonation transition). In the numerical simulation in § 4.2, we will address this problem further. Additionally, the centred rarefaction waves cannot be identified clearly because of the weak density gradients and the schlieren photograph sensitive to the first density derivatives. In figures 5(*c*) and 5(*d*), the vortex ring is faintly visible just after the detonation diffracts around point L.

In figure 5(*e*), the leading shock front approaches the right-hand corner (point B), and the reflection immediately occurs. In figure 5(*f*), regular reflections appear on both the bottom wall in the horizontal branch and the right-hand wall in the vertical branch. Owing to the serious influence of the centred rarefaction waves from point L, the leading shock in the vertical branch attenuates steeply because of the decrease of the pressure and temperature behind it. Since the chemical reaction rate is strongly dependent on the temperature, lower temperature results in a relatively slower reaction rate and a much longer induction zone. Therefore, the reaction front in the vertical branch has been separated further from the leading shock and it is seriously wrinkled. A cell-free region 4 is indicative of the separation of the leading shock and reaction zone or detonation failure. In figure 5(*g*), regular reflection has transitioned into Mach reflection in the horizontal branch. The reflected shock can be clearly seen around point B. In the vertical branch, because the reflected shock further increases the pressure and temperature and then stimulates rapid chemical reactions, a re-initiation occurs behind the reflected shock. Local explosions induced

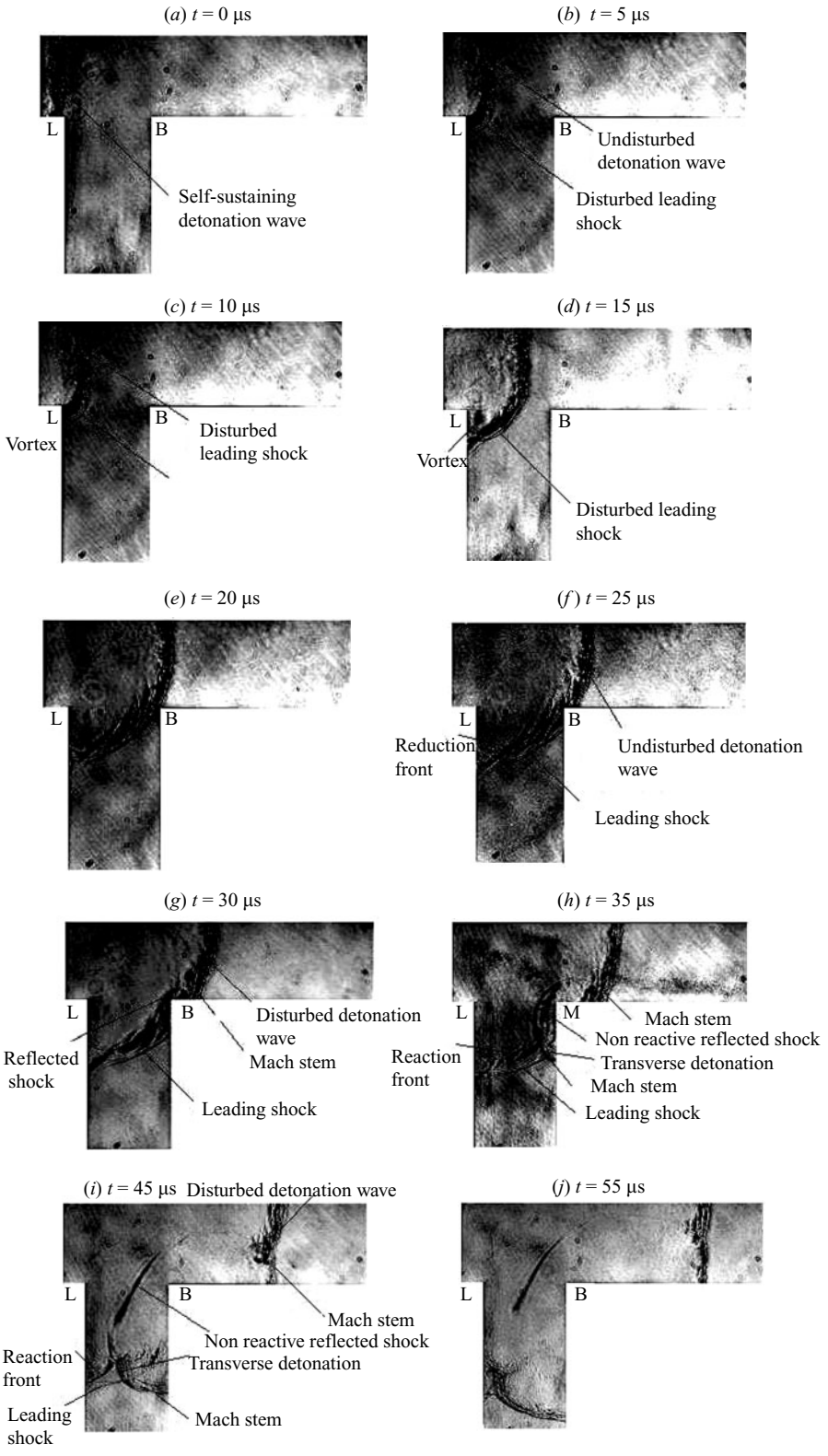

FIGURE 5. Schlieren images in a bifurcated tube ($2H_2 + O_2 + Ar$, $p_0 = 16.00\,\text{kPa}$).

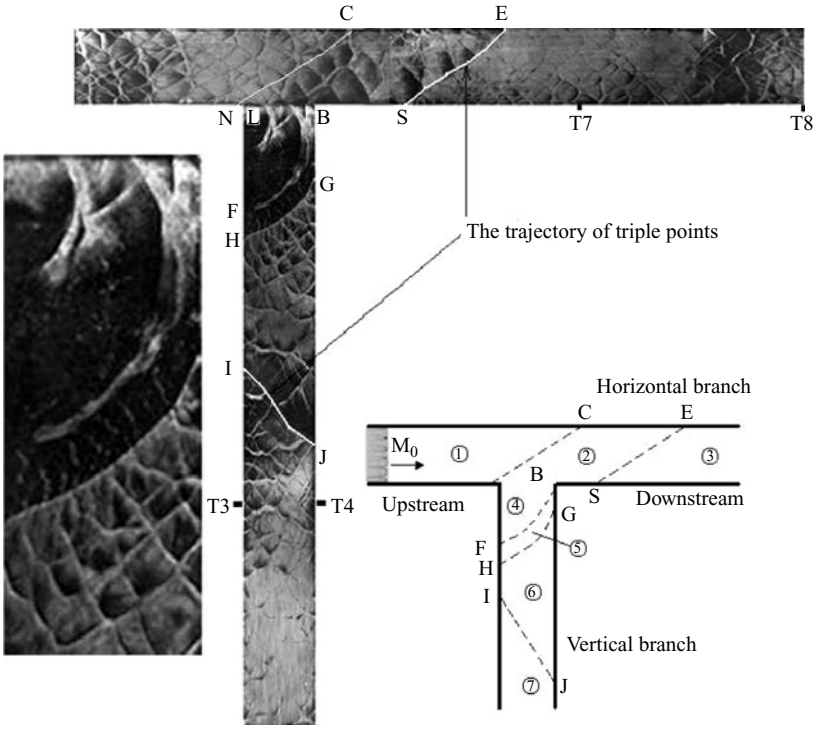

FIGURE 6. Cellular pattern and related regions in a bifurcated tube ($2H_2 + O_2 + Ar$, $p_0 = 16.00$ kPa) (*a*) Locally enlarged cellular pattern; (*b*) cellular pattern; (*c*) related regions.

by this re-initiation strengthen the reflected shock and stimulate the fast recouping of the reaction zone and reflected shock that propagates in the unreacted mixture. In figure 5(*h*), regular reflection has also transitioned into Mach reflection in the vertical branch. The reflected shock can be divided into two portions. One is referred to as the transverse detonation wave, which propagates transversely into the unburnt but shocked mixtures between the leading shock and reaction zone; the other one is referred to as the non-reactive reflected shock, which travels into the completely reacted mixtures. The transverse waves of the transverse detonation wave faintly identified in figure 5(*h*) are very dense so that they give rise to the fine cells in region 5 in figure 6. The non-reactive reflected shock, transverse detonation wave and decoupled reaction front intersect at a triple point which scrapes a dividing line between the cell-free region and fine cell region on the smoked foil. This dividing line, which starts from a uncertain point between points B and G on the right-hand wall and terminates at point F on the left-hand wall, is obvious on the cellular pattern. At the same time, the detonation re-initiation occurs. The trajectory of triple points in the process of Mach reflection marks another dividing line GH in figure 6. The detonation wave in the Mach stem region is also temporarily overdriven and the cell sizes in the neighbourhood of GH are smaller than the equilibrium cell sizes representative of the self-sustaining detonation wave. This overdriven Mach stem detonation wave decays and the cell sizes increase. In figures 5(*i*) and 5(*j*), in the vertical branch, because the Mach stem detonation wave propagates faster than the left-hand separated leading shock, it catches up with and then exceeds the leading shock. When the Mach stem meets the left-hand wall, another Mach reflection occurs.

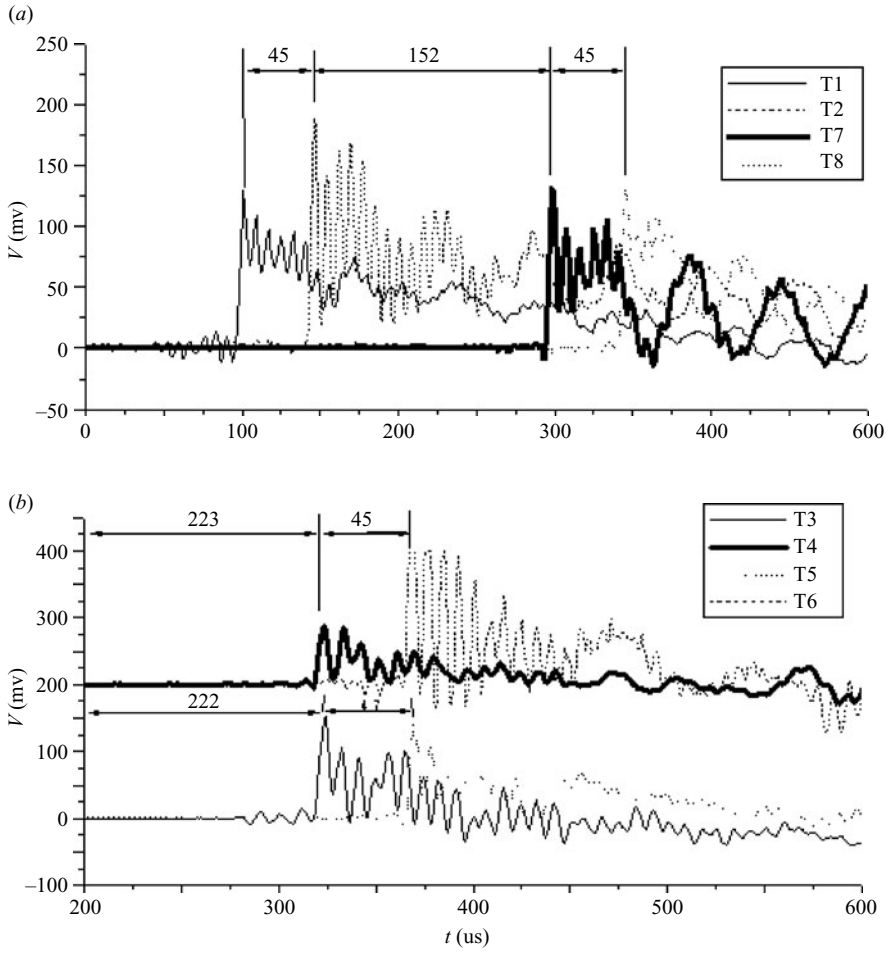

FIGURE 7. Typical pressure profiles ($2H_2 + O_2 + Ar$, $p_0 = 16.00$ kPa).

Line IJ denotes the trajectory of triple points. Downstream of region 7, the detonation wave gradually recovers, and almost the same cell sizes as the equilibrium cell sizes in region 1 can be observed in figure 6. In the horizontal branch, the Mach stem has extended its length and its reaction zone is much thinner than that of the disturbed incident detonation because the strong Mach stem detonation wave induces high temperature as well as rapid reaction rates. Line DE in figure 6 denotes the trajectory of triple points. Because of the sharp pressure increase behind the Mach stem, the cell sizes on both sides of SE are remarkably different. Downstream of region 3, owing to the non-sustaining behaviour of the Mach stem detonation wave, the detonation wave in the completely increased Mach stem region decays to a self-sustaining cellular detonation wave with the same cell sizes as those in region 1.

Figure 7 presents the details of pressure profiles from eight transducers at the initial pressure of 16.00 kPa, where t denotes the time and V denotes the voltage relative to the pressure. As shown in figure 1, the transducers T1 and T2 are located upstream of the bifurcated segment, where the detonation wave propagates in a self-sustaining manner. Currently, the transducer cross-section is small compared with the detonation cell, and therefore the pressure maximum measured by the transducer is changeable

Initial pressure (kPa)	D_{CJ}	Detonation T1–T2	T2–T7	T7–T8	Average T3–T5	Speed ($m\,s^{-1}$) T4–T6	T2–T3
10.67	2167	2128	2044	2128	2083	2222	1746
13.33	2177	2128	2070	2128	2128	2222	1784
16.00	2185	2128	2044	2128	2083	2222	1765
18.67	2192	2174	2124	2174	2128	2222	1844
20.66	2196	2174	2152	2174	2128	2222	1813

TABLE 2. Average speed of the gaseous detonation wave in a bifurcated tube at different p_0.

even for the self-sustaining detonation wave. Thus the measured maximum pressure value is not reliable for determining whether the detonation wave is degenerated, enhanced or failing. T7 is placed 125 mm downstream of the right-hand corner B in the horizontal branch, and the disturbed detonation wave is closely recovered to a self-sustaining one. T3 or T4 is 150 mm, and T5 or T6 is 250 mm away from the horizontal branch, respectively. Corresponding to figure 6, all pressure profiles are indicative of the detonation wave. Based on the distances between two neighbouring transducers and time intervals of the corresponding profiles, it is easy to calculate the average speeds of detonation propagation. The obtained average speeds at different initial pressure p_0 are presented in table 2. The average speed of the self-sustaining detonation wave is slightly lower than the calculated CJ value (Gordon & McBride 1971). This is attributed to the chemical reaction proceeding at a finite rate and the energy losses on the tube wall and viscous boundary layer. In the vertical tube, its average speed increases at the right-hand wall, owing to the occurrence of the re-initiation and the transition from regular reflection to Mach reflection. However, along the left-hand wall, the detonation wave is evidently decelerated becuase of the effect of the rarefaction waves. In the horizontal tube, the average speeds are slightly different from that of self-sustaining detonation wave. Downstream of the location of T8, the disturbed detonation wave is already restored to a self-sustaining one, whereas it still requires some time to recover in the vertical branch.

Figures 8 and 9 show the schlieren images in the bifurcated tube filled with the same mixtures at different initial pressure. The evolution of wavefronts is very similar to those shown in figure 5. It is also found that, with increasing initial pressure, the width of the induction zone decreases and the influence of the bifurcated segment on detonation wave is weakened. Therefore the distorted detonation wave returns to a self-sustaining one increasingly earlier downstream of the vertical or horizontal branch.

Figures 10 and 11 show the cellular patterns in the vertical and horizontal branches at different initial pressure. The cellular pattern evolution and the mechanism of detonation propagation are also similar to those presented in figure 6. However, with increasing initial pressure, the start point S of Mach reflection in the horizontal branch becomes closer to the right-hand corner B. This indicates that higher initial pressure promotes the resistance of the detonation wave against the effect of rarefaction waves and therefore facilitates the fast recovery of the disturbed detonation wave to a self-sustaining one. The distance required for recovery is about 2–4 times the tube height in the horizontal tube, whereas it is about 3–6 times the tube height in the horizontal tube.

A typical cellular pattern under the critical condition is presented in figure 12. Here, the critical condition denotes the detonation failure in the horizontal or vertical branch. When p_0 drops to 2.00 kPa, a self-sustaining detonation wave with only one

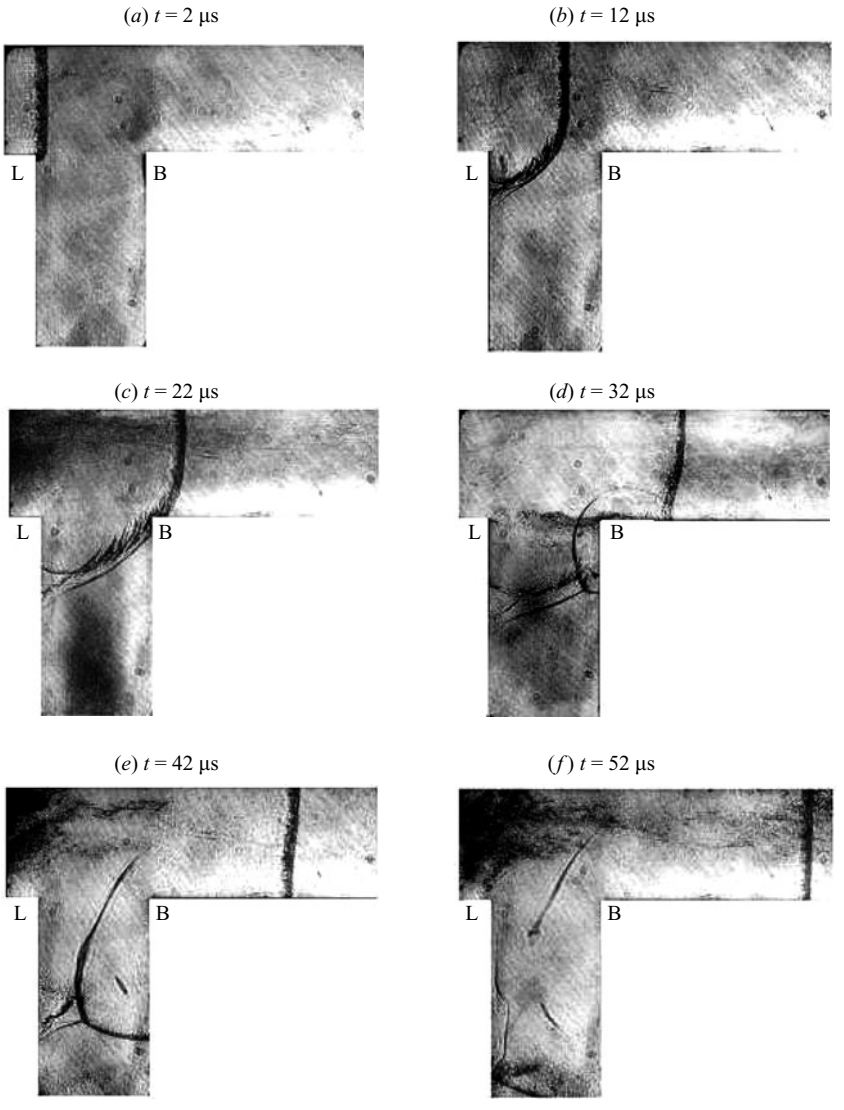

FIGURE 8. Schlieren images in a bifurcated tube ($2H_2 + O_2 + Ar$, $p_0 = 26.67$ kPa).

or two transverse waves can be formed upstream of the bifurcated segment, and therefore it is very close to a marginal detonation wave. In the horizontal branch, the cell sizes are first larger than and then equal to the equilibrium cell sizes. This indicates that the self-sustaining detonation can be re-established from the disturbed one; but the boundary NC and the trajectory of triple points SE in figure 6 canot be identified clearly in figure 12. Absence of a cellular pattern in the vertical branch indicates detonation failure owing to the serious effects of centred rarefaction waves from point L. The current experiments also indicate, if p_0 is below 2.00 kPa, the self-sustaining detonation wave cannot be successfully generated upstream of the bifurcated segment.

Because of the limitation of the 720 μs time delay of the ruby laser and the distance between the spark plug and the pressure transducer T2 which is used to trigger

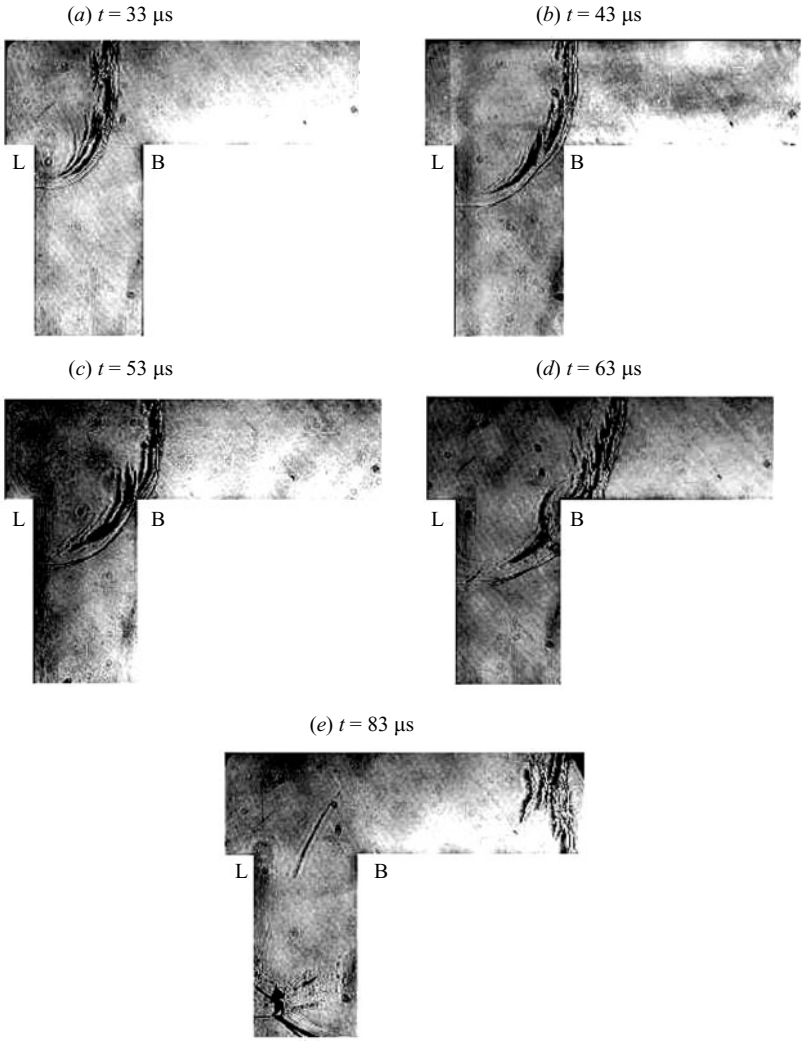

FIGURE 9. Schlieren images in a bifurcated tube ($2H_2 + O_2 + Ar$, $p_0 = 10.67$ kPa).

the ruby laser, as the initial pressure drops below 10.67 kPa, the transition from deflagration to detonation cannot be finished upstream of this trigger transducer. This results in an uncertain delay time, and therefore the schlieren images under the critical condition are not obtained.

4.2. *Numerical results*

Figure 13 shows a series of numerical schlieren and temperature contours illustrating detonation evolution in a bifurcated tube at different times. The self-sustaining cellular detonation wave upstream of the bifurcated segment has a quasi-regular transverse-wave structure containing 11 triple points and producing approximately 5.5 detonation cells. When detonation enters the bifurcated segment, the rarefaction waves, which emanate from point L, interact with the leading shock and cause the disturbed part to decay. It was found that the separation of the wrinkle reaction zone from the leading shock is evident in the vertical branch, owing to the absence of a sustained energy release from the chemical reaction. Several bottom triple points are faintly visible

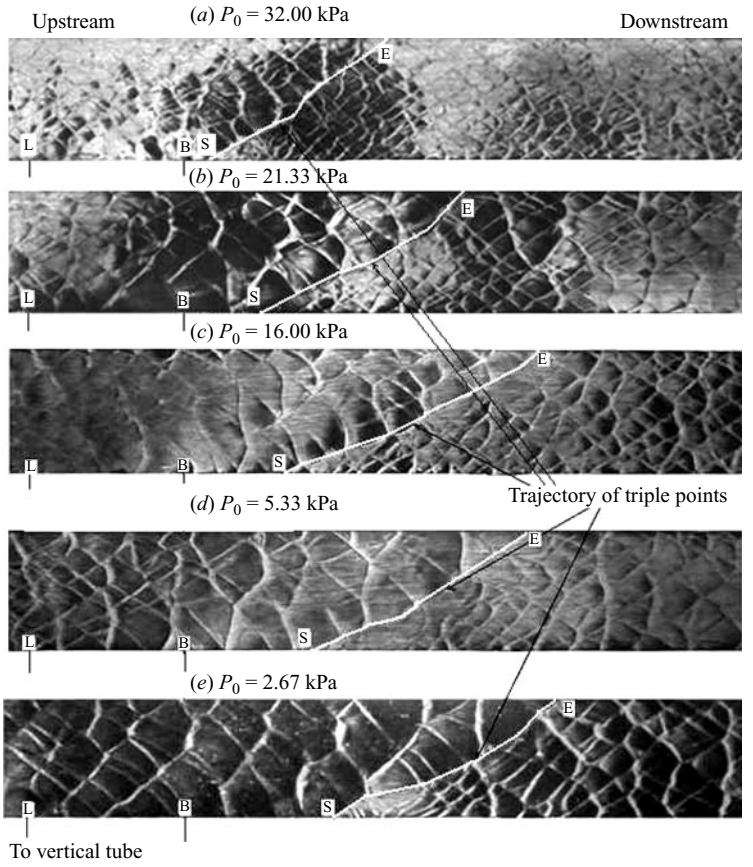

FIGURE 10. Cellular patterns in the horizontal branch at different initial pressure ($2H_2+O_2+Ar$).

along the leading shock front in figures 13(*b*) or 13(*c*); however, they are inert and cannot imprint a triple-point trajectory on smoked foil. So it is appropriate to say that detonation fails around the left-hand corner in the vertical branch. The average speed of wall shock at the left-hand wall has dropped to about 0.45 of the average speed of self-sustaining detonation wave.

The subsequent behaviour of detonation re-initiation in figures 13(*d*) to 13(*f*) is of considerable interest. At the rear of the reflected shock is an induced region with high pressure and temperature of about three times CJ detonation pressure and 1.2–1.3 times CJ detonation temperature, respectively. It is well known that the chemical reaction rate is strongly dependent on the temperature. Such high temperature in the unburn mixtures compressed by the leading shock stimulates violently exothermic chemical reactions and the presence of hot spots. High OH mass fraction at the rear of the reflected shock is easily observed in figure 14(*a*). For a hydrogen–oxygen mixture, OH radicals are yielded as an intermediate product by the chain-branching reaction, representative of the reaction zone structure. A high OH concentration area generates no (or very short) induction delay to the reflected shock, which indicates that the reaction zone is coupled with the reflected shock and they propagate together in an overdriven manner. All these provide information on the occurrence of the

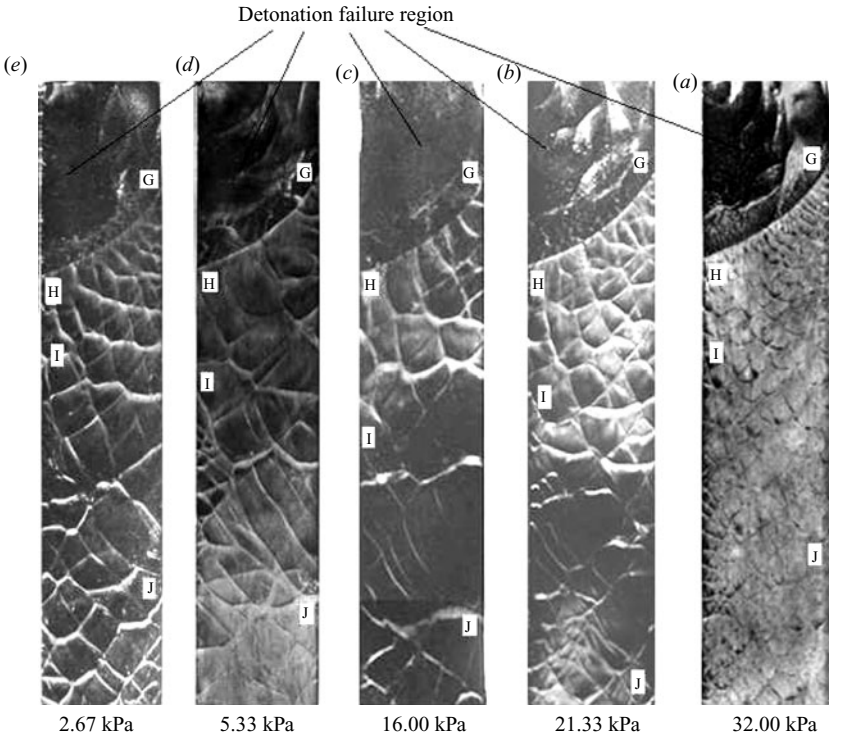

FIGURE 11. Cellular patterns in the vertical branch at different initial pressure ($2H_2 + O_2 + Ar$).

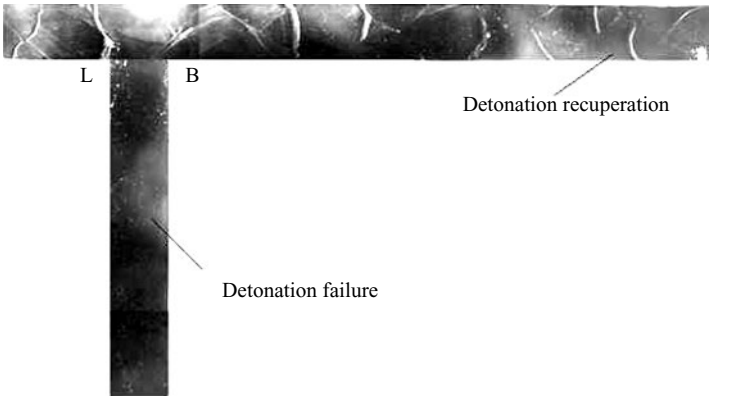

FIGURE 12. Cellular pattern under the critical condition ($2H_2 + O_2 + Ar$, $p_0 = 2.00$ kPa).

detonation re-initiation. As reported by Ohyagi *et al.* (2002) and Li & Kailasanath (2000), this re-initiated wave is an overdriven detonation wave.

Numerical simulation also shows that, in both horizontal and vertical branches, the leading shock undergoes the transition from regular reflection to Mach reflection. It is worth noting that, in the case of such reflection, this behaviour of the gaseous detonation wave is somewhat different from that of a non-reactive shock wave (Igra *et al.* 1998). As for the latter, just after passing through the right-hand corner, the shock wave exhibits a pure Mach reflection in the horizontal branch and experiences

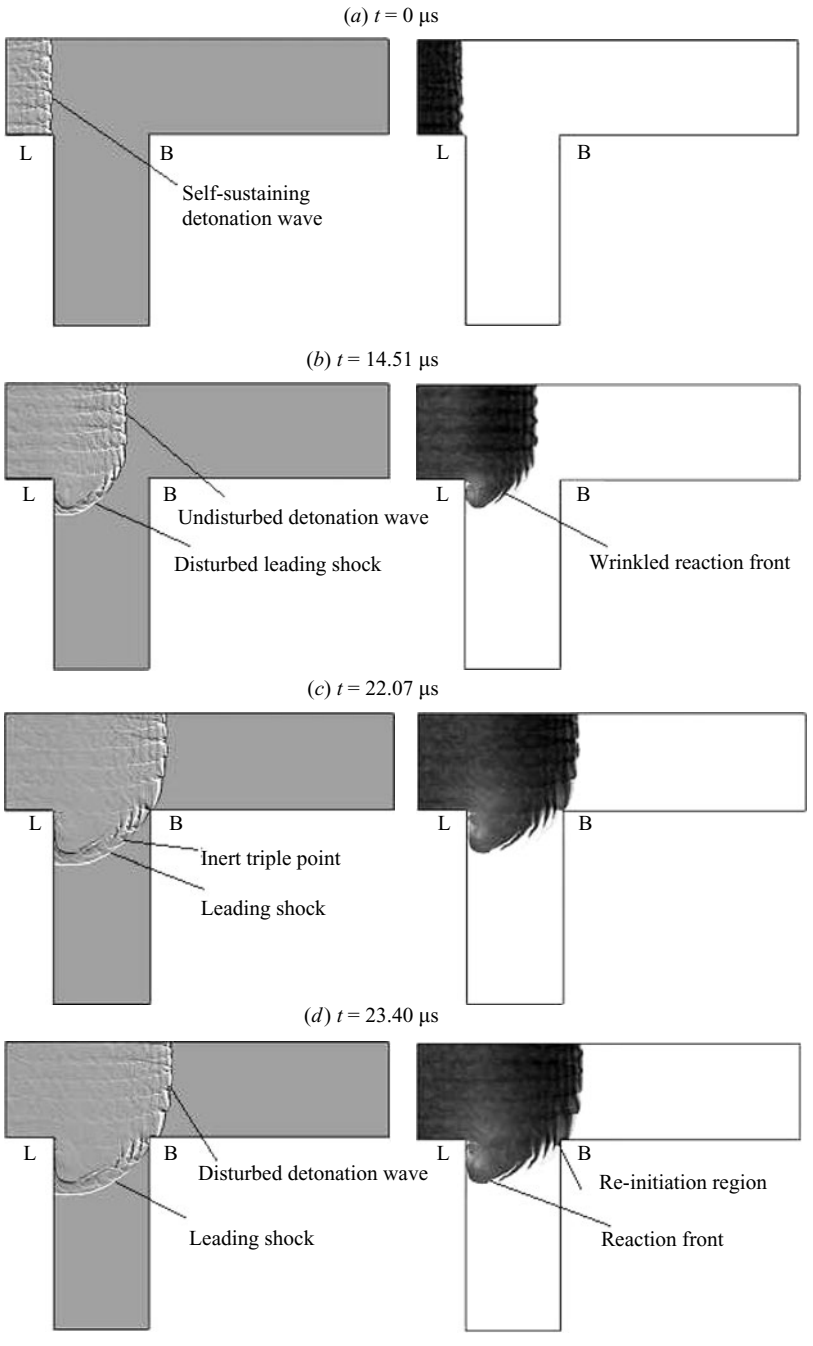

FIGURE 13(*a–d*). For caption see facing page.

the transition from the regular reflection to Mach reflection in the vertical branch. In the current study, the Mach stem is macro-scale and includes one or many micro-scale Mach stems in a cellular detonation structure. In figure 14(*b*), a high OH concentration area is generated behind the Mach stem, which indicates that strongly exothermic reactions occur and therefore induce high temperature and pressure. The induction delay between the OH concentration front and the corresponding leading

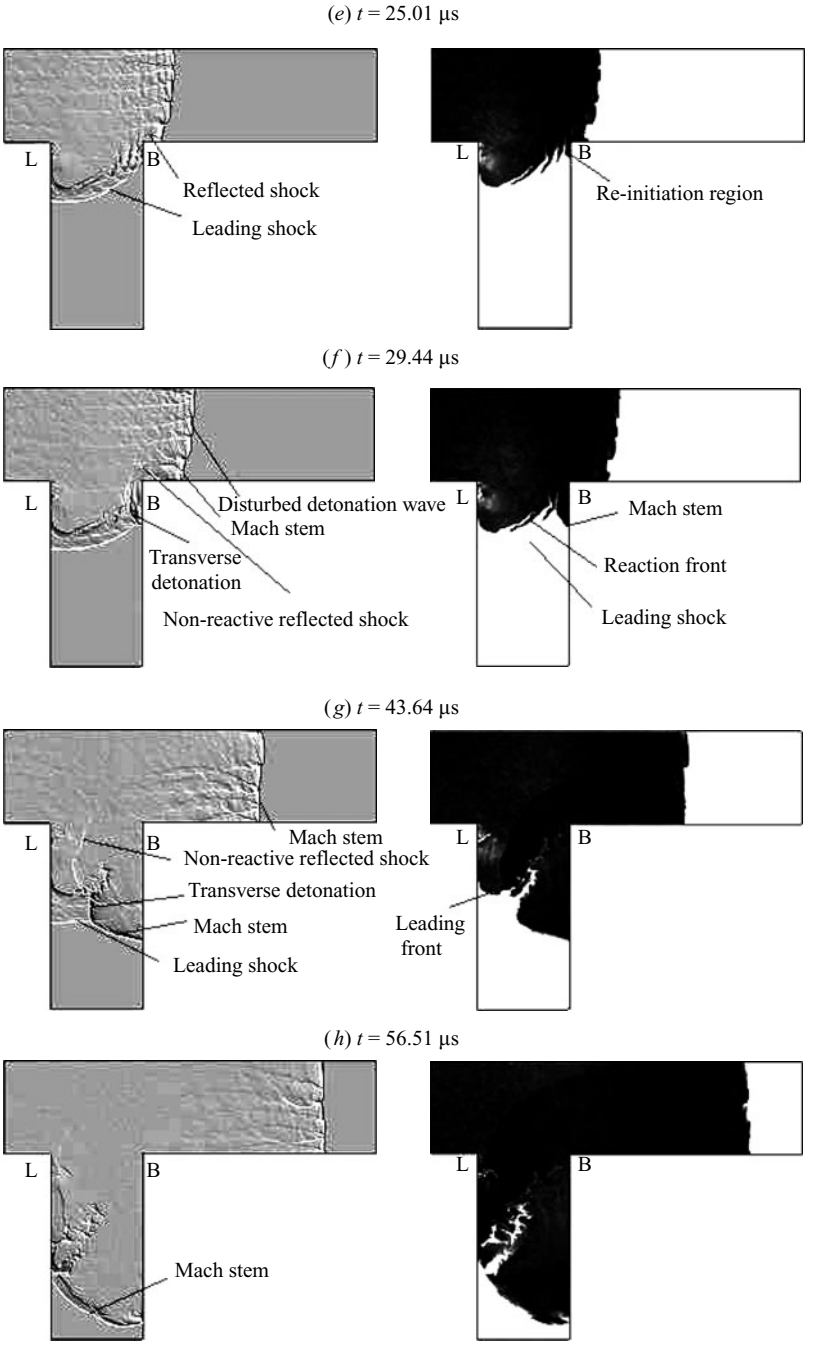

FIGURE 13. Numerical schlieren (left-hand side) and temperature (right-hand side) contours of detonation evolution in a bifurcated tube ($2H_2 + O_2 + Ar$, $p_0 = 8.00\,\mathrm{kPa}$).

shock front are shortened. This facilitates the growth of the Mach stem and then the recovery to the self-sustaining cellular detonation wave.

Figure 15 shows locally enlarged vorticity and temperature contours around the left-hand corner (point L) at selected times. In figure 15(*a*), the cellular detonation diffracts

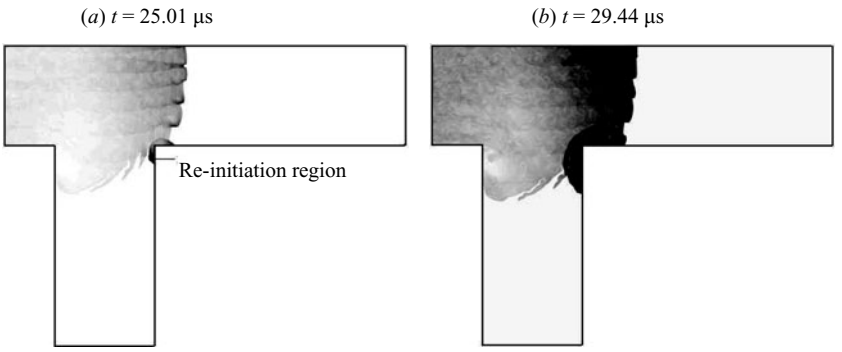

FIGURE 14. OH mass fraction contours at given time ($2H_2 + O_2 + Ar$, $p_0 = 8.00\,\text{kPa}$).

around point L. Because of the effects of rarefaction waves from point L, the reaction zone is gradually decoupled with the leading shock. The acceleration of supersonic flow behind the leading shock, owing to the abrupt area expansion, produces a contact discontinuity CD1. CD1 originates from the left-hand corner and deflects clockwise. It separates the flow at low speed creeping along the left-hand wall of the vertical branch, from the flow at higher speed coming from the upstream region of the bifurcated segment. Another contact surface CD2 which deflects counterclockwise, surrounds CD1 and follows the leading shock. It separates the reacted materials from the unburnt but shocked materials. An unreacted recirculation region stretches close to point L along CD2 and the left-hand wall of the vertical branch. A secondary shock, required to match the high pressure behind the leading shock and the low post-rarefaction pressure, can be discerned. In figure 15(*b*), a clockwise vortex V1 is wrapped by CD1. Close to point L, CD2 develops another small counter-vortex V2. V1 and V2 can be clearly identified in vorticity contour. The temperature contour indicates that, in the centre of V2, partially reacted materials are convolved. Some unreacted but shocked materials from the recirculation region penetrate the completely burnt materials along CD1. As the leading shock propagates forwards, the flow around point L decelerates, and even transits from supersonic to subsonic flow. In figure 15(*c*), the deceleration of the flow disturbs CD1, and induces its instability. As a result, CD1 is twisted and CD2 develops another vortex V3 which rotates counterclockwise. The emergence of vortex V3 causes the recirculation region to be cut into two parts U1 and U2. In figure 15(*d*), several clockwise vortices emerge and they are all tied on CD1. In figure 15(*e*), these vortices are detached from each other and their structures become chaotic. Vortex V2 has completely dissipated and then disappeared. In the process of interaction with V2, the unreacted U2 are gradually consumed. In figure (*f*), owing to the gradually enlarged structure of V3, the tail of U1 is peeled off the left-hand wall and stretches deeply into the reacted mixtures. U2 is seriously wrinkled and recombined with U1. The reflected shock RS1 can be clearly seen. In figure 15(*g*), RS1 passes through the vortex system of CD1, referred to as shock–vortex interaction. RS1 compresses and breaks these vortices. In figure 15(*h*), a portion of RS1 close to the leading shock reflects off the left-hand wall. Because of high temperature and pressure behind RS1 or secondary reflected shock RS2, the accelerated chemical reactions consume most of the unreacted materials in the recirculation region U1. The unreacted portion of U1 and the high temperature and pressure products are developed as a right-facing jet. This phenomenon is more evident in figure 15(*i*). As this embedded jet spreads, its head becomes a mushroom-like structure.

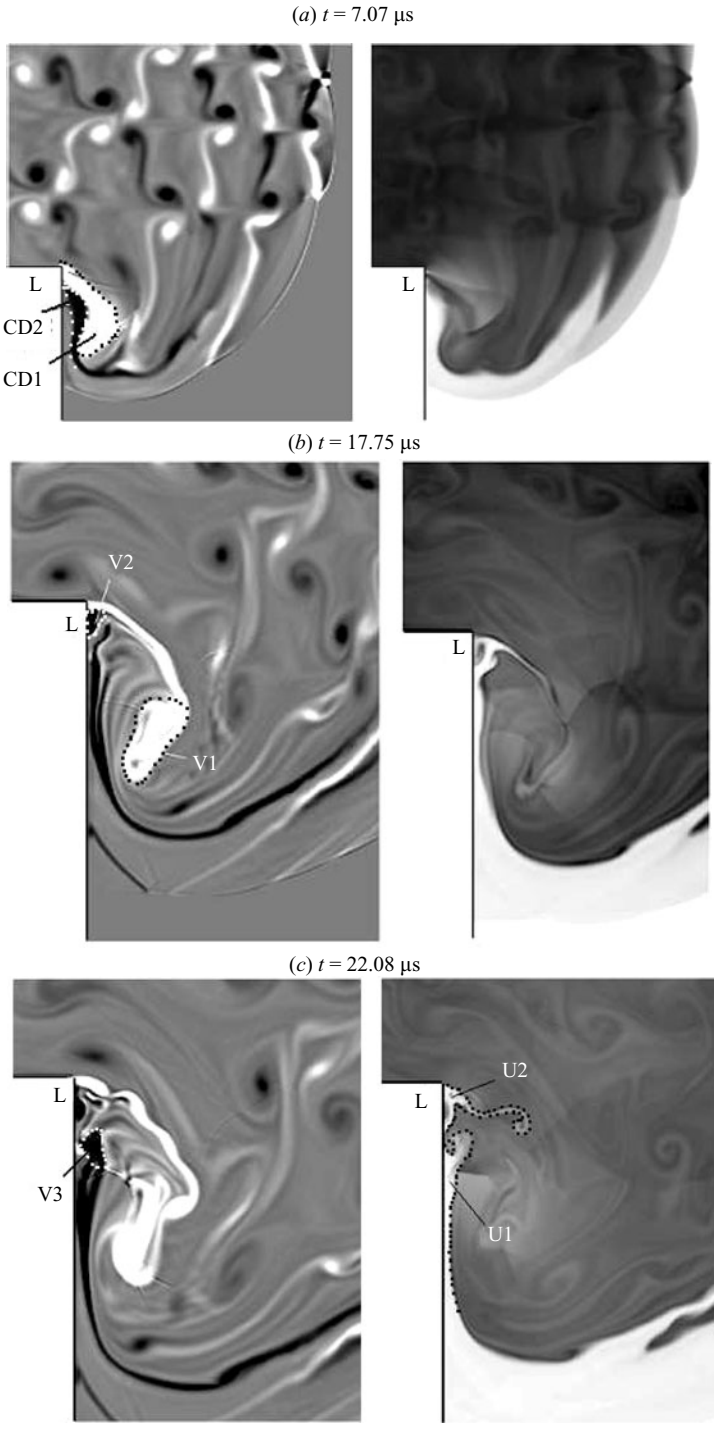

FIGURE 15(*a–c*). For caption see p. 101.

As described in figures 15(*h*) to (*i*), the hot and rapidly burning materials are squeezed by the left-hand wall and curved reflected shocks into a right-facing jet. Certainly, this jet is not a conventional one that forms when continuous liquid or gas

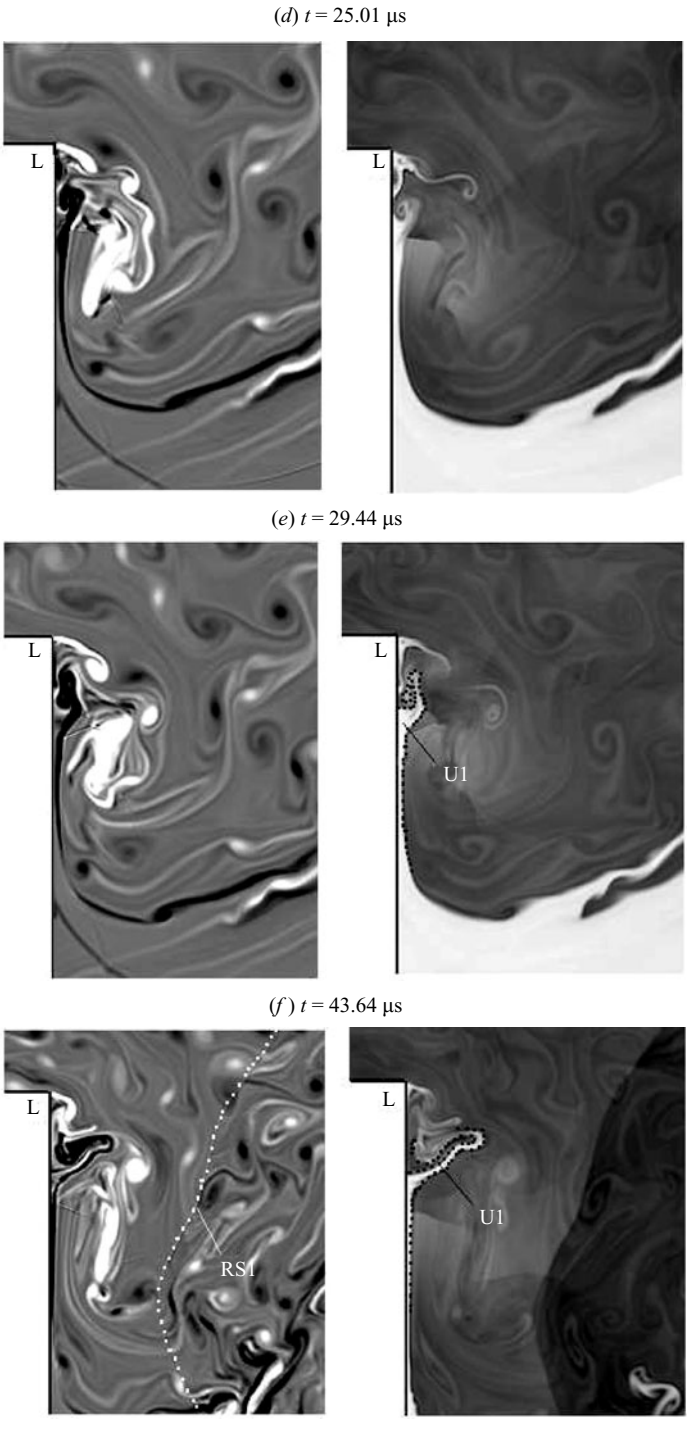

FIGURE 15(*d*–*f*). For caption see facing page.

is injected into a gas medium through a small nozzle or hole. Since it involves chemical reactions in the unreacted materials and reacted products, it is also different from the wall-jet in Mach reflection in a non-reactive flow (Henderson *et al.* 2003;

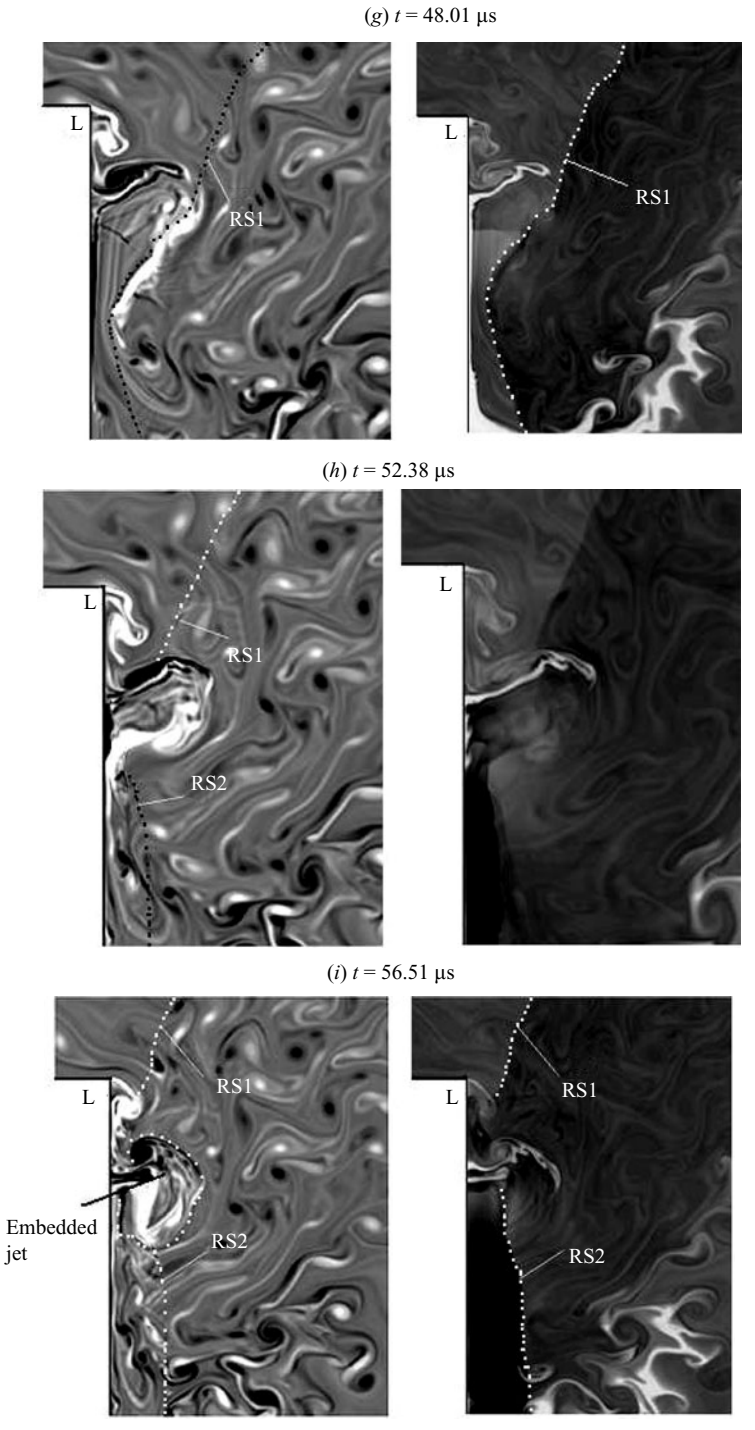

FIGURE 15. Locally enlarged vorticity (left) and temperature (right) contours, the artificial dotted curves highlight vortex, embedded jet, recirculation region and reflected shock.

Vasilev *et al.* 2004). Figure 16 presents the evolution of the enlarged jet around the left-hand corner. In figure 16(*a*), LUM is the low-temperature unreacted mixture. It is originally a part of the recirculation region which then peeled off the left-hand wall, owing to new vortex emergence and flow degeneration. In this mixture, its temperature is about 3–5 times the initial temperature. As it evolves, its head first becomes a mushroom-like structure. Owing to the reflection of reflected shock RS1 on the left-hand wall, the resultant RS3 is formed. Furthermore, a new jet is generated close to the left-hand wall. In figures 16(*b*) and 16(*c*), this jet appears as a cylinder with a hemispherical head. As it evolves further, the jet develops a mushroom-like structure and induces two vortices around its head. Influenced by LUM, the vortex and mushroom-like structure on the top left-hand side of the jet head is much compressed; however, they obtain enough stretch and evolution on the top right-hand side. All these can be easily seen in figures 16(*d*) to 16(*f*). This jet, combined with LUM, develops a large mushroom-like structure in figure 15(*i*).

Analysing parameter distribution along the jet can assist in understanding the jet characteristics and instability. Figure 17 presents Mach number distribution along the jet. Note that, here, Mach number is the ratio of the local velocity to the local acoustic velocity. It is found that, at the initial stage of jet formation, such as $t = 55.40\,\mu s$, the reflected shock RS3 induces the supersonic flow in front of the jet. Across the jet head, this supersonic flow is accelerated to Mach number 2.0. At $t = 56.51\,\mu s$, the jet nearly catches up with RS3, and its head Mach number is about 2.1. As time elapses, even though the supersonic flow in front of the jet transits to subsonic flow, it changes to supersonic across the jet head again. It is evident that the supersonic region inside the jet reduces. The jet maximum Mach number is not decreased or increased monotonously, but pulsates. So it is approximate to say that the jet is unstable. Even though such behaviour prevails in the whole process of jet spreading, the maximum value of the flow Mach number in the jet decreases. Additionally, at any selected time, the Mach number, from jet head to tail, increases dramatically to a maximum value and then gradually decays. At the jet tail, the flow is subsonic, and furthermore its velocity decreases to $0\,m\,s^{-1}$ owing to the viscous left-hand wall effect.

As described in figure 13, the transition from regular reflection to Mach reflection occurs in the vertical branch. Here, we will address the Mach stem characteristics in detail. In the Mach stem region an overdriven detonation wave is induced. It is well known that this Mach stem detonation wave cannot propagate in a self-sustaining manner. Its overdrive degree usually decays, which finally leads to the formation of a self-sustaining detonation wave. Figure 18 presents the Mach number curve of Mach stem detonation along the right-hand wall versus the distance away from the right-hand corner. Note that, here, the Mach number is the ratio of the Mach stem detonation wave velocity to the acoustic one in front of it. It is found that the maximum value of the Mach number is about 7.8, much higher than that of the conventional CJ detonation wave. This also indicates that the re-initiation induces the local violent energy release and an extremely strong Mach stem detonation wave. Then this Mach stem detonation exhibits its non-sustaining behaviour, and its Mach number drops with some slight fluctuations. These fluctuations may be attributed to its intrinsic nature. Additionally, the grid resolution also results in the uncertainty of the location of the Mach stem in a grid of size Δx. After the Mach stem detonation wave exhibits a minimum travelling velocity, owing to a new triple-point generation on the Mach stem, this triple point collides with the right-hand wall, which results in a Mach number steep increase of the Mach stem detonation wave. Figure 19

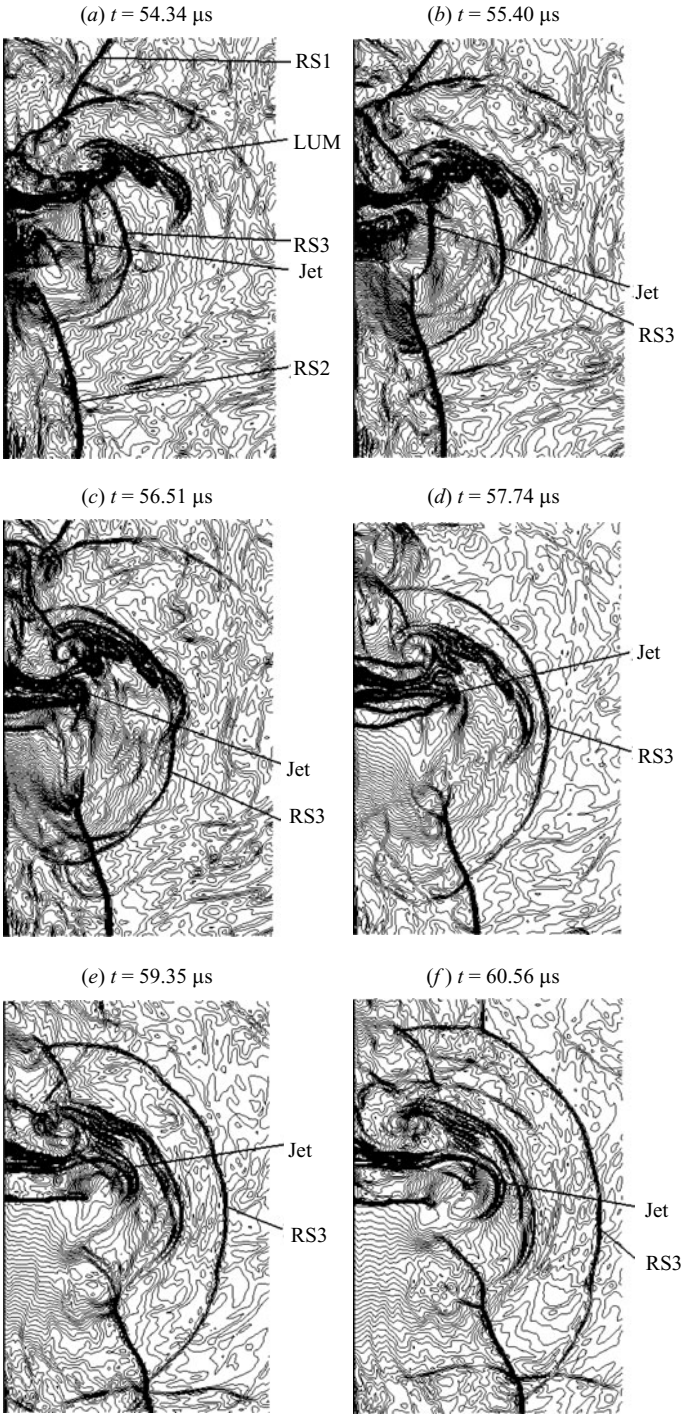

FIGURE 16. Density distributions of the enlarged jet.

presents the evolution of the Mach stem configuration in the vertical branch. As for the non-reactive Mach stem in steady flows, Tan, Ren & Wu (2006) found that the configuration of the Mach stem is approximated well by an arc with very small

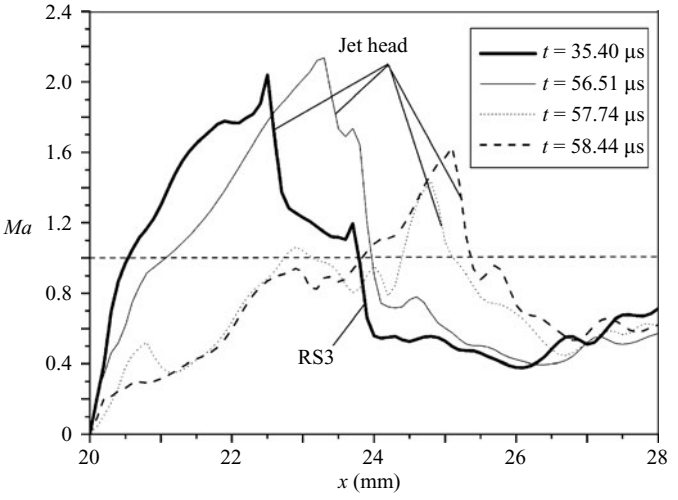

FIGURE 17. Mach number distributions along the jet at different time.

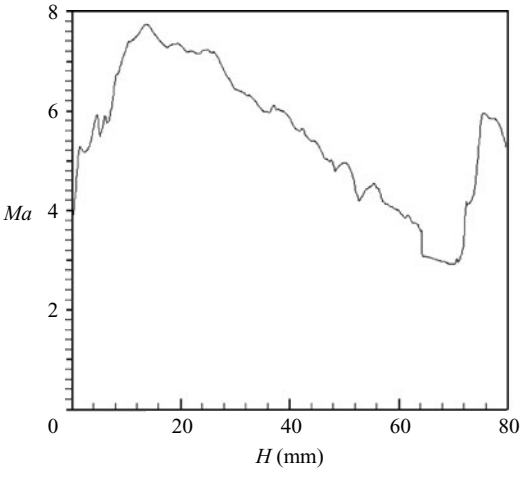

FIGURE 18. Mach number evolution of Mach stem detonation along the right-hand wall.

curvature. For a reactive Mach stem in the current study, it appears that, at the initial stage, the Mach stem is just like an arc. However, along with the Mach stem growing, the configuration of the Mach stem is gradually changed. Especially when the new triple point is generated at $t = 52.38\,\mu s$, the Mach stem configuration is seriously distorted and cannot be approximated as an arc. The preliminary explanation is as follows. Because of the influence of the rarefaction waves emitted from the left-hand corner L, the Mach number at different points along the leading front, especially along the portion in the vertical branch, is different. Therefore, the corresponding point on the Mach stem also has a different Mach number. Relatively, the leading shock close to the right-hand wall is affected by the rarefaction waves less than that close to the left-hand wall. Thus, in the vicinity of the right-hand wall, the separation between the leading shock and reaction zone is not serious and the difference in Mach number at every point on the leading shock is relatively smaller. So the initially formed Mach stem seems to be an arc. With increasing Mach stem, the difference of

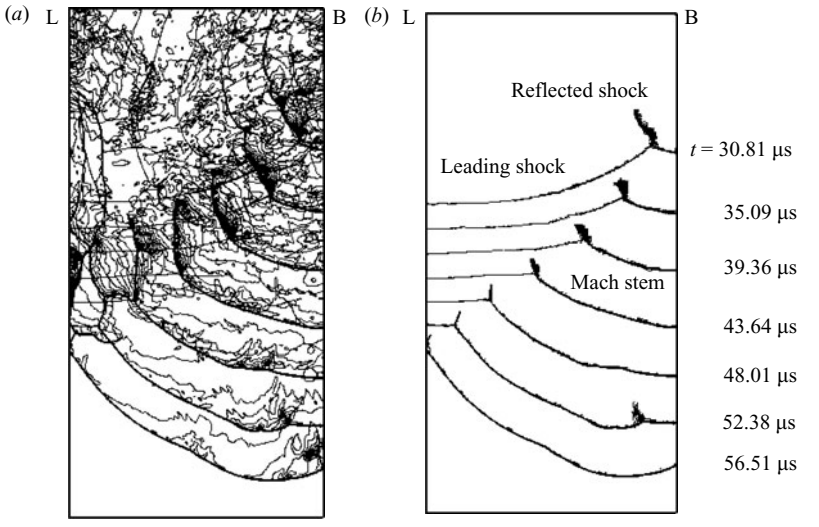

FIGURE 19. Mach stem evolution in the vertical branch. (*a*) Snap shots of Mach stem. (*b*) Schematic of Mach stem.

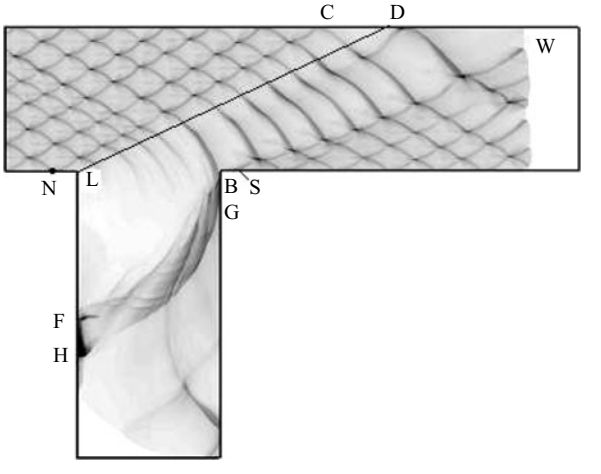

FIGURE 20. The time history of pressure maximum value at $p_0 = 8.00\,\mathrm{kPa}$.

Mach number on the leading shock and Mach stem is more evident. Furthermore, the Mach stem detonation wave will develop its triple points. These result in the serious distortion of the Mach stem configuration. So, in unsteady reactive flows, the Mach stem strength varies at any point and any moment. Therefore its configuration cannot be approximated as an arc. This behaviour is evidently different from that of the Mach stem in non-reactive steady flows (Tan *et al.* 2006).

Figure 20 shows the time history of the pressure maximum value which is representative of the numerical cellular pattern at $p_0 = 8.00\,\mathrm{kPa}$. Upstream of the bifurcated segment, the cells closer to uniform than elsewhere in the system are indicative of the self-sustaining detonation wave. Owing to the effects of the rarefaction waves emitted from the left-hand corner L, and also owing to the decaying and disappearing of transverse waves in the wake of the left-hand corner, the larger

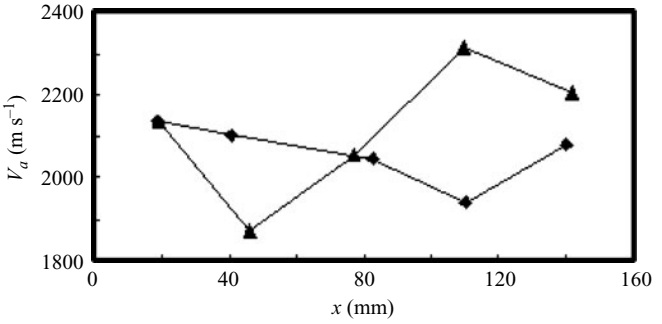

FIGURE 21. Average detonation speed V_a along ALBK (▲) and MN (◆) versus distance x.

detonation cells can be found. NC is the boundary line between uniform and larger cells. Line LD is the first characteristic line of rarefaction waves. Point N is usually upstream of point L. There exists a special case where point N is just at point L only when the initial self-sustaining detonation structure is suitably imposed. In the horizontal branch, a trajectory of triple points SW is evident, on both sides of which the cell shape and size are remarkably different. It denotes the onset of Mach reflection. Mach reflection starts not at the right-hand corner, but at the point S which is downstream of the right-hand corner. In the vertical branch, the cell-free region and the re-initiation zone are easily identified. Moreover, much finer cells in the re-initiation zone provides a proof for the overdriven transverse detonation wave. The starting point of the re-initiation is in the vicinity of point B, and its accurate position is also uncertain.

The average detonation speed V_a along MN is plotted versus the distance x away from point G in figure 21. The average speed of the self-sustaining detonation is 2125.0 m s^{-1}. With increasing distance, the average detonation speed decreases owing to the effect of the rarefaction waves from the left-hand corner L. After exhibiting the minimum value, it rises, which indicates that the degenerated detonation wave can be recovered. Figure 21 also shows the average detonation speed V_a along ALBK versus the distance x away from A. The rarefaction waves rapidly decrease the average detonation speed. When degenerated detonation approaches the right-hand corner B, the regular reflection and subsequent Mach reflection occur. This leads to the rapid increase of the average detonation speed. Owing to the non-sustaining nature of the Mach stem detonation wave, it decays close to the average speed of the self-sustaining detonation wave.

The average speed of the leading shock along LP is plotted versus the distance H away from point L in figure 22. It shows that the rarefaction waves from point L strongly decrease the average speed of the leading shock. At the point that is about 60 mm away from the left-hand corner L, the transverse detonation approaches the left-hand wall. Then Mach reflection occurs and the average speed of the leading shock is sharply increased. Figure 22 also shows the average detonation speed along BQ versus the distance H away from point B. When the diffracted leading shock reaches the right-hand corner, detonation re-initiation results in a steep increase of the average detonation speed. The speed, which is about 2600 m s^{-1} at distance of about 20 mm from the right-hand corner, indicates that the re-initiated detonation wave is overdriven. Here, the regular reflection of the leading shock is also transitioned to Mach reflection. Because of its non-sustaining behaviour, the speed of the overdriven Mach stem detonation wave gradually decays.

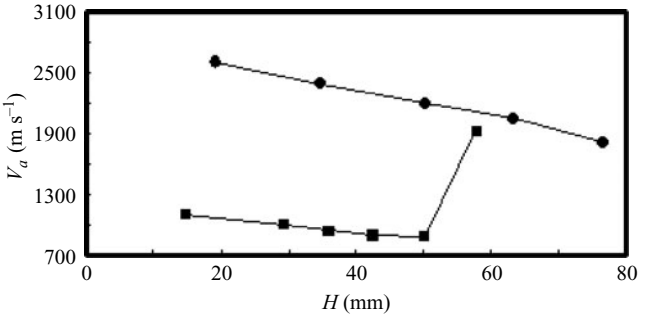

FIGURE 22. Average detonation speed V_a along LP (■) and BQ (●) versus distance H.

4.3. *Comparison between numerical and experimental results*

Numerical simulation based on the reactive Navier–Stokes equations served to elucidate the detonation phenomena in the bifurcated tube. The turbulent effects were ignored in the computation. In addition, the adiabatic wall boundary condition was employed. This means that the gas temperature in the tube determines the wall temperature. In the experiments, the walls are usually not as hot as the gas in high-velocity reactive flow. Hence, there exist the energy losses on cold walls and the relatively thicker viscous boundary layer in experiments. As a result, in the same straight tube, the experiments usually show larger detonation cells than the simulation (Oran *et al.* 1998; Eckett 2001). In the current numerical simulation, the self-sustaining detonation wave at the initial pressure of 8.00 kPa has an almost identical cellular pattern and triple-point number to those obtained at 16.00 kPa in experiments. Additionally, experience has shown that, with increasing initial pressure, the grid size must be much finer in order to obtain converged or equilibrium self-sustaining cellular detonation. For example, the grid size is 0.1 mm and the total grid number is 960 000 for an initial pressure of 8.00 kPa, whereas the grid size drops to 0.04 mm and the total grid number reaches 6 000 000 for an initial pressure of 16.00 kPa. For consideration of computational efficiency, the initial pressure of 8.00 kPa is chosen for the current numerical simulation. So only qualitative comparison between numerical and experimental results is carried out. In this paper, numerical simulations are expected to reproduce the detonation wave evolution observed in the experiments and reveal fundamental details which help us to recognize the related dynamics.

The centred rarefaction waves around the left-hand corner L are barely seen in both numerical and experimental schlieren images, since the schlieren system is sensitive to the first density derivatives which are quite small in the rarefaction fan region. As shown in figure 13, affected by the rarefaction waves emitted from point L, the reaction zone is separated from the leading shock. Owing to the inert leading-shock reflection on the right-hand wall in the vertical branches, the re-initiation occurs, with the presence of high pressure, high temperature and high OH mass fraction behind the reflected shock. These observations help us to obtain insight into experimental phenomena in figure 5. The locations of points N, S and the start point of the re-initiation have a certain random nature in figure 20. This is attributed to the initial location of the imposed detonation wave and the characteristics of the cellular structure. Here, the former is randomly imposed, corresponding to that arising from the randomness of DDT in experiments. The latter means the cell size and the curvature shape of the cell boundary. This random phenomenon of the locations of these points is also observed in the experiments. In general, the computed wave

evolution is in qualitative agreement with that from the experiments. Furthermore, the wave position evolution at 8.00 kPa in the simulation is quantitatively consistent with that at 16.00 kPa in the experiments (see figures 5 and 13). In contrast with experimental schlieren images, the numerical schlieren images show the shock wave and reaction front more clearly. In the experiments, the integration effect of the schlieren system along the light direction and three-dimensional structures of the detonation wave creates the image integrating and fogging.

By comparing the numerical and experimental cellular patterns (figures 6 and 20), a striking difference to note is that, in the vertical branch, the real experiments present more and finer detonation cells in the Mach stem region than the numerical simulation. In the numerical simulation, the Mach stem detonation has a short induction zone and is overdriven (see figure 13). There are not enough transverse waves perturbing the leading shock front to generate the triple points and further form the detonation cells. This phenomenon may be attributed to no consideration of turbulent effects and the current computational grid size being insufficient for this overdriven detonation caused by the Mach stem. In a word, the numerical cellular pattern reflects clearly the mechanism of detonation diffraction through a branched segment. The detonation wave sequentially experiences attenuation, local failure, overdriven re-initiation and recuperation, etc. Strictly speaking, numerical simulation is consistent with real experiments qualitatively under available conditions.

5. Conclusions

Experimental and numerical studies were carried out on gaseous detonation propagation in a bifurcated tube. The pressure transducer, smoked foil and laser schlieren visualization were used in the current experiments for obtaining the pressure history, cellular pattern and detonation front image, respectively. The tested gas mixture was $2H_2 + O_2$ with 25% argon dilution at different initial pressure. The computation was based on reactive Navior–Stokes equations with a detailed chemical reaction model. The fifth-order WENO scheme was used to resolve the convective term and the second-order additive semi-implicit Runge–Kutta method was employed to treat the stiffness caused by the chemical source. The viscosity, thermal conduction and molecular diffusion terms were evaluated using second-order central finite difference. The computations were performed with the currently investigated mixture only at an initial pressure of 8.00 kPa.

The experimental and numerical results show that the detonation wave is strongly influenced by the wall geometry of the bifurcated tube. The rarefaction waves from the left-hand corner result in detonation failure. Re-initiation occurs owing to the leading shock reflection on the right-hand wall of the vertical branch. Regular and Mach reflections sequentially occur in both horizontal and vertical branches. In the vertical branches, the detonation wave experiences degeneration, failure, re-initiation, and transition from regular reflection to Mach reflection twice. In the horizontal branch, the detonation wave is still maintained despite its attenuation. The boundary between the regions of relatively uniform and larger cells is not the first characteristic line of rarefaction waves, and its starting point does not start exactly at the left-hand sharp corner and is usually upstream of it. Also, the starting point of the triple-point trajectory characterizing Mach reflection is usually located downstream of right-hand corner in the horizontal branch. It is found in the experiments that as the initial pressure is equal to or more than 2.67 kPa, the disturbed detonation wave can recover to a self-sustaining wave at a distance of about 2–4 times the tube wall height in

the horizontal branch, and 3–6 times in the vertical branch. As p_0 drops to 2.00 kPa, the self-sustaining detonation wave is only recovered downstream of the horizontal branch, but the detonation wave fails in the vertical branch.

Numerical simulation also shows that complex vortex structures, shock–vortex interaction and the unreacted recirculation region etc. are observed around the left-hand corner. The reflected shock interacts with the vortices and breaks them into pieces. The interaction of reflected shock and the unreacted recirculation region results in an embedded jet. This jet is unstable and spreads in a supersonic manner at the initial stage. As for the Mach stem in the vertical branch, the strength of it at any point is different and furthermore varies with time. Therefore the Mach stem configuration is seriously distorted and cannot be approximated as an arc. This behaviour is evidently different from that of the Mach stem in non-reactive steady flow. In general, the numerical simulation qualitatively reproduces the experimental phenomena and reveals fundamental details which help us to recognize the related characteristics of detonation propagation in a bifurcated tube.

This work was sponsored by National Natural Science Foundation of China (Grant 10172083), China Postdoctoral Science Foundation (Grant 2005037167) and Open Foundation of State Key Laboratory of Explosion Science and Technology of Beijing Institute of Technology (Grant KFJJ03-2,KFJJ04-2).

The authors express sincere thanks to the editor, Professor Norbert Peters, and the reviewers for many insightful comments and suggestions.

REFERENCES

Akbar, R. 1997 Mach reflection of gaseous detonations. PhD thesis, Rensselaer Polytechnic Institute, New York.

Arienti, M. & Shepherd, J. E. 2005 A numerial study of detonation diffraction. *J. Fluid Mech.* **529**, 117–146.

Bartlmä, F. & Schröder, K. 1986 The diffraction of a plane detonation wave at a convex corner. *Combust. Flame* **66**, 237–248.

Bourlioux, A., Majda, A. J. & Roytburd, V. 1991 Theoretical and numerical structure for unstable one-dimensional detonations. *SIAM J. Appl. Maths* **51**, 303–343.

Eckett, C. A. 2001 Numerical and analytical studies of the dynamic of gaseous detonation. PhD thesis. California Institute of Technology.

Edwards, D. H. & Thomas, G. O. 1979 The diffraction of a planar detonation wave at an abrupt area change. *J. Fluid Mech.* **95**, 79–96.

Gordon, S. & McBride, D. J. 1971 Computer program for a calculation of complex chemical equilibrium compositions rockets performance incident and reflected shocks Chapman–Joudguet detonations. *NASA SP*.

Guo, C. M., Zhang, D. L. & Xie, W. 2001 The Mach reflection of a detonation based on soot track measurements. *Combust. Flame* **127**, 2051–2058.

Guo, C., Thomas, G., Li, J. & Zhang, D. 2002 Experimental study of gaseous detonation propagation over acoustically absorbing walls. *Shock Waves* **11**, 353–359.

Henderson, L. F., Vasilev, E. I., Ben-Dor, G. & Elperin, T. 2003 The wall-jetting effect in Mach reflection: theoretical consideration and numerical investigation. *J. Fluid Mech.* **479**, 259–286.

Igra, O., Wang, L., Palcovitz, J. & Heilig, W. 1998 Shock wave propagation in a branched duct. *Shock Waves* **8**, 375–381.

Jones, D. A., Kemister, G., Tonello, N., Oran, E. S. & Sichel, M. 2000 Numerical simulation of detonation re-ignition in H_2–O_2 mixtures in area expansions. *Shock Waves* **10**, 33–41.

Li, C. P. & Kailasanath, K. 2000 Detonation transmission and transition in channels of different sizes. In *28th Symp. (Intl) on Combustion*, pp. 603–609. The Combustion Institute.

Ohyagi, S., Obara, T., Nakata, F. & Hoshi, S. 2000 A numerical simulation of reflection processes of a detonation wave on a wedge. *Shock Waves* **10**, 185–190.

Ohyagi, S., Obara, T., Hoshi, S., Cai, P. & Yoshihashi, T. 2002 Diffraction and re-initiation of detonations behind a backward-facing step. *Shock Waves* **12**, 221–226.

Oran, E. S., Young, T. R. & Boris, J. P. 1982 Weak and strong ignition. Numerical simulations of shock tube experiments. *Combust. Flame* **48**, 135–148.

Oran, E. S., Weber, J. W., Stefaniw, E. I., Lefebvre, M. H. & Anderson, J. D. 1998 Numerical study of a two-dimensional H_2–O_2–Ar detonation using a detailed chemical reaction model. *Combust. and Flame* **113**, 147–163.

Radulescu, M. I. & Lee, J. H. S. 2002 The failure mechanism of gaseous detonation: experiments in porous wall tubes. *Combust. Flame* **131**, 29–46.

Schultz, E. 2000 Detonation diffraction through an abrupt area expansion. PhD thesis. California Institute of Technology.

Shu, C. W. 1997 Essentially non-oscillatory and weighted essentially non-oscillatory schemes for hyperbolic conservation laws. *ICASE Rep.* 97-65.

Shu, C. W. & Osher, S. 1988 Efficient implementation of essentially non-oscillatory shock capturing schemes I. *J. Comput. Phys.* **77**, 439–471.

Shu, C. W. & Osher, S. 1989 Efficient implementation of essentially non-oscillatory shock capturing schemes II. *J. Comput. Phys.* **83**, 32–78.

Tan, L. H., Ren, Y. X. & Wu, Z. N. 2006 Analytical and numerical study of the near flow field and shape of the Mach stem in steady flows. *J. Fluid Mech.* **546**, 341–362.

Thomas, G. O. & Williams, R. L. 2002 Detonation interaction with wedges and bends. *Shock Waves* **11**, 481–492.

Vasilev, E. I., Ben-Dor, G., Elperin, T. & Henderson, L. F. 2004 The wall-jetting effect in Mach reflection: Navier–Stokes simulations. *J. Fluid Mech.* **511**, 363–379.

White, D. R. 1961 Turbulent structure of gaseous detonation. *Phys. Fluids* **4**, 465–479.

Zhong, X. L. 1996 Additive semi-implicit Runge–Kutta methods for computing high-speed noneqilibrium reactive flows. *J. Comput. Phys.* **128**, 19–31.

Zhou, K. Y. & Li, Z. F. 1997 The quenching of propane–air deflagrations by narrow parallel channels. *Explosion Shock Waves* **17**, 112–118.

Zhou, K. Y., Li, Z. F. & Chen, Z. J. 1990 Experimental investigations on the stability of equilibrium cellular structures in gaseous detonation. *Explosion Shock Waves* **10**, 129–134.